

MAGNETOSPHERIC ACCRETION MODELS FOR THE HYDROGEN EMISSION LINES OF T TAURI STARS

JAMES MUZEROLLE

Five College Astronomy Department, University of Massachusetts, Amherst, MA 01003; jamesm@inyo.phast.umass.edu

AND

NURIA CALVET¹ AND LEE HARTMANN

Harvard-Smithsonian Center for Astrophysics, Mail Stop 42, 60 Garden Street, Cambridge, MA 02138;
ncalvet@cfa.harvard.edu, hartmann@cfa.harvard.edu

Received 1997 June 11; accepted 1997 August 21

ABSTRACT

Using a statistical equilibrium radiative transfer treatment, we examine the behavior of hydrogen emission lines arising from the magnetospheric infall zones of classical T Tauri stars. Having calculated self-consistent line profiles of the Balmer lines, $\text{Pa}\beta$ and $\text{Br}\gamma$, we explore parameter space, examining the effects of the magnetospheric gas temperature and size on the line fluxes. We compare model and observed line fluxes for the Balmer lines and find a good match using a relatively small range of parameters. We are also able to match the observed $\text{Br}\gamma$ line profile of the embedded object WL 16, which supports the use of the infrared lines in studying magnetospheric infall even in the earliest stages of star formation. Finally, we discuss constraints on the physical parameters and the possibility of using the emission lines as accretion rate indicators.

Subject headings: accretion, accretion disks — line: profiles — radiative transfer — stars: pre-main-sequence

1. INTRODUCTION

Recent theoretical work on accretion in classical T Tauri stars (CTTSs) has moved away from the standard boundary layer model in favor of magnetospheric accretion (Königl 1991; Shu et al. 1994; Calvet & Hartmann 1992; Hartmann, Hewett, & Calvet 1994, hereafter HHC). In this model, the stellar magnetic field truncates the disk at some inner radius, and accretion continues onto the star by gas infall along magnetic field lines connecting the star to the disk near the truncation radius. The infalling gas is at free-fall velocities when it strikes the photosphere at high latitudes, forming an “accretion” shock where most of the kinetic energy is dissipated by X-ray and EUV emission. Since the gas is very optically thick, the short-wavelength radiation is almost immediately absorbed and reemitted at longer wavelengths, giving rise to the optical and ultraviolet excess continuum emission that is observed (Bertout, Basri, & Bouvier 1988; Gullbring et al. 1998, hereafter GHBC). If accretion occurs in discrete magnetic “columns,” or if the magnetic field is not aligned with the stellar rotation axis, the resulting hot spots on the photosphere could account for the photometric variations seen in some CTTSs (Simon, Vrba, & Herbst 1990; Bouvier et al. 1993, 1995; Herbst, Herbst, & Grossman 1994). Kenyon et al. (1994) in particular employ the magnetospheric accretion model to explain the hot spot on DR Tauri.

This magnetospheric model explains the features of observed line profiles in CTTSs. Most of these stars exhibit strong emission lines with large line widths and occasional inverse P Cygni (IPC) profiles (the YY Orionis stars: Walker 1972; Appenzeller & Wolf 1977; Edwards 1979, Edwards et al. 1994). In particular, the presence of redshifted absorption components at velocities up to several hundred kilometers per second indicates infall from rela-

tively large distances. Edwards et al. (1994) present high-resolution spectroscopy of the Balmer lines for a sample of CTTSs in Taurus, revealing convincing infall signatures in many of the stars. If the disk is truncated and accretion continues along magnetic field lines, the infalling gas will be on an essentially ballistic trajectory, falling onto the star at nearly free-fall velocities. The boundary layer picture (where disk accretion occurs all the way to the photosphere) cannot produce the high velocities necessary to be consistent with the observed IPC line profiles.

Radiative transfer modeling of Balmer line profiles from CTTSs has strengthened the case for magnetospheric accretion. Hartmann et al. (1990) and Calvet, Hartmann, & Hewett (1992) computed line profiles with spherical and conical, respectively, outflowing wind models. The results could not reproduce the broad and nearly centrally peaked profiles that have been observed, nor could they explain the presence of redshifted absorption components. HHC obtained much more consistent results by using a magnetospheric infall model, idealized to the case of an axisymmetric dipole field geometry. The resultant profiles exhibit the large line widths and central peaks typically observed. HHC also found that the presence of a redshifted absorption component is determined largely by geometry and the detailed behavior of the line source function and is not a requisite of the infall picture (consistent with the fact that a small fraction of CTTSs do not show evidence of IPC structure in their Balmer emission lines—see Edwards et al. 1994). The calculated absorption is also deeper in the higher Balmer lines, which is again consistent with the observations.

The results of HHC were limited by the assumption of two-level atomic models. In this paper, we remove this restriction by considering a multilevel hydrogen atom in statistical equilibrium. With this improved method, we are able to calculate self-consistently many line profiles and fluxes in addition to the Balmer series. We explore param-

¹ Also Centro de Investigaciones de Astronomía, Mérida, Venezuela.

eter space, investigating the roles gas temperature, magnetosphere size, and accretion rate play in the production of the hydrogen emission lines. We also compare the model results with observations of CTTSs in Taurus, with the ultimate goal of obtaining spectral diagnostics for the accretion rate and the size and temperature of the magnetosphere. Such diagnostics would be especially important for the study of CTTSs in embedded clusters, where the standard methods for determining accretion rates are not applicable.

2. METHOD

2.1. Physical Model

The physical model used in HHC is retained here; see that paper for the quantitative details. The magnetosphere is assumed to be a dipole field, axisymmetric about the star's rotation axis and perpendicular to the disk (see Fig. 1 for a schematic diagram). The disk, with a truncated inner radius that also corresponds to the innermost field line (and is a free parameter), is taken to be opaque and nonemitting at all frequencies. The stellar parameters of mass, radius, and photospheric temperature are fixed at typical T Tauri star values ($0.5 M_{\odot}$, $2 R_{\odot}$, and 4000 K, respectively; GHBC). Figures 2 and 3 show the velocity, density, and temperature distributions for two reference cases. We neglect rotation, since typical T Tauri star rotation rates are considerably less than the velocities of the infalling gas (15 km s^{-1} vs. 200 km s^{-1}). This may introduce considerable uncertainty in the parts of the line profile near line center if the magnetosphere rotates rigidly with the star, since that emission arises near the disk, where the infall velocity is comparable to the rotation velocity. Nevertheless, most of the profile will remain unaffected, and we leave this complication to a future study.

2.2. Radiative Transfer

We employ an extended Sobolev radiative transfer method, applicable in the case of large, nonmonotonic velocity gradients (Rybicki & Hummer 1978). This is appropriate for the emission lines from T Tauri stars, where line

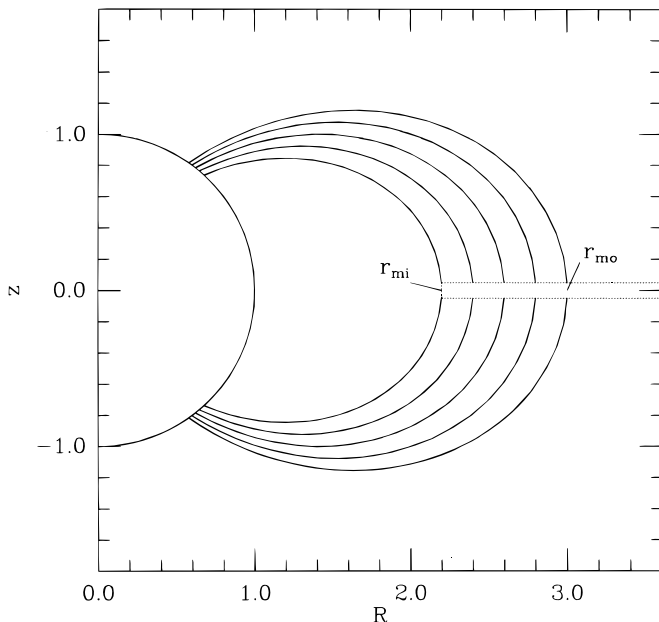


FIG. 1.—The dipole field geometry used in the magnetospheric accretion model (from HHC).

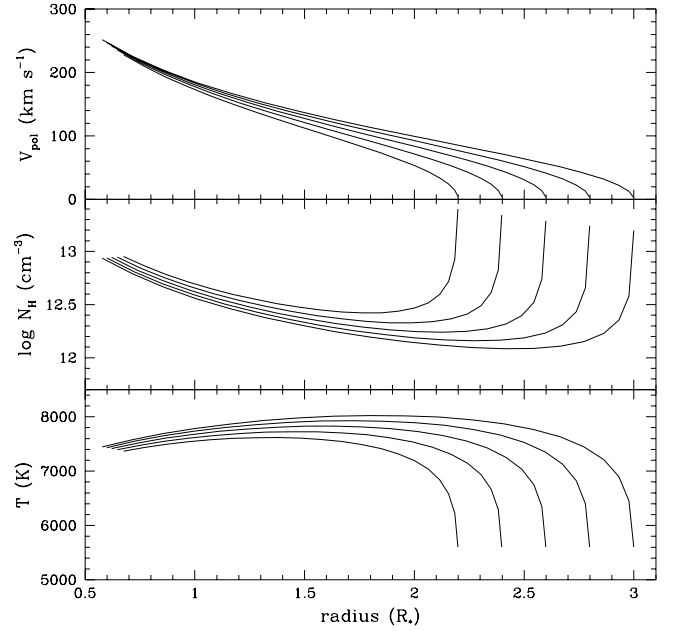


FIG. 2.—Velocity, density, and temperature distributions for a fiducial case: $\dot{M} = 10^{-7} M_{\odot} \text{ yr}^{-1}$, $T_{\text{max}} = 8000 \text{ K}$, $R_* = 2 R_{\odot}$, $M_* = 0.5 M_{\odot}$, $r_{\text{mi}} = 2.2 R_{\odot}$, and $r_{\text{mo}} = 3 R_{\odot}$.

widths are typically several hundreds of kilometers per second, and thus the gas flow is highly supersonic. The radiation field is calculated over a grid of 100 points that covered the entire length of the infall region from disk to stellar surface. At each point r , the mean intensity is given by

$$\bar{J}_v = [1 - \beta(r)]S(r) + \beta_c(r)I_c + F(r), \quad (1)$$

where $\beta(r)$, $\beta_c(r)$, $S(r)$, and $F(r)$ are the local and continuum (photosphere plus accretion shock) escape probabilities, source function, and nonlocal emission, respectively, at r , in

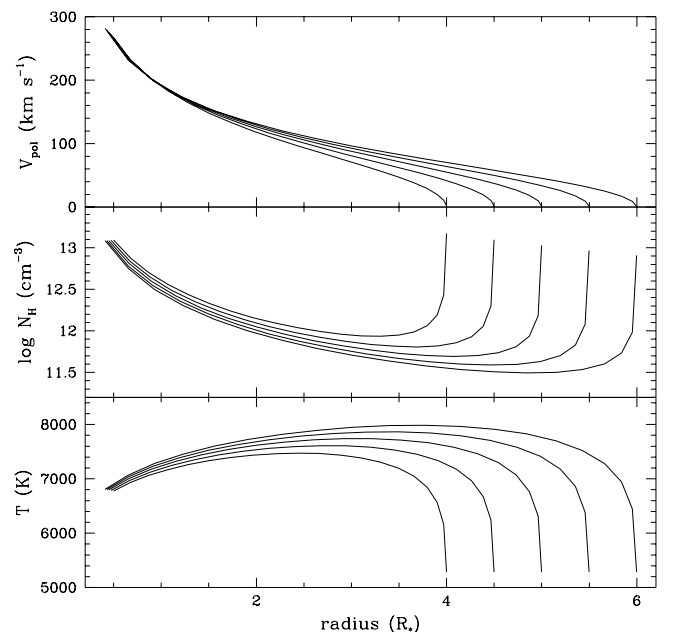


FIG. 3.—Velocity, density, and temperature distributions for a larger magnetosphere: $\dot{M} = 10^{-7} M_{\odot} \text{ yr}^{-1}$, $T_{\text{max}} = 8000 \text{ K}$, $R_* = 2 R_{\odot}$, $M_* = 0.5 M_{\odot}$, $r_{\text{mi}} = 4 R_{\odot}$, and $r_{\text{mo}} = 6 R_{\odot}$.

turn given by

$$\beta(r) = \frac{1}{4\pi} \int d\Omega(n) \frac{1 - \exp[-\tau(r, n)]}{\tau(r, n)}, \quad (2)$$

$$\beta_c(r) = \frac{1}{4\pi} \int d\Omega(n) \frac{1 - \exp[-\tau(r, n)]}{\tau(r, n)} \exp\left[-\sum_{i=1}^N \tau(r, n)\right], \quad (3)$$

$$F(r) = \frac{1}{4\pi} \int d\Omega(n) \frac{1 - \exp[-\tau(r, n)]}{\tau(r, n)} \times \sum_{i=1}^N S(r_i) \{1 - \exp[-\tau(r_i, n)]\} \exp\left[-\sum_{j=1}^{i-1} \tau(r_j, n)\right]. \quad (4)$$

The line optical depths, $\tau(r_i, n)$, are determined from the line opacities and velocity gradients at each point, r , and direction, n (see HHC). The integrals are taken over all solid angles, $d\Omega$, around n . The “core” term, $\beta_c I_c$, is actually split into two terms, one integrated over the solid angle of the photosphere and the other integrated over the solid angle of the hot accretion ring. The core specific intensities are taken as blackbodies at the photospheric and accretion ring temperatures. Finally, the flux per unit frequency is

$$F_\nu = \sum_k \sum_l r_k dr_k d\phi_l \left\{ \sum_i S_i(r_k, \phi_l) \times \exp\left[-\sum_{j=1}^{i-1} \tau(r_j, m)\right] \{1 - \exp[-\tau(r_i, m)]\} + I_c \exp\left[-\sum_{i=1}^N \tau(r_i, m)\right] \right\}, \quad (5)$$

with the sums over the interacting constant velocity surfaces, i and j , where r_k and ϕ_l are polar coordinates measured relative to the center of the star, perpendicular to the line of sight, m . (See HHC and Rybicki & Hummer 1978 for more details.)

2.2.1. The Line Source Function

In order to obtain the emergent flux, we must first determine the source function at each point on the grid. HHC solved the transfer equations using a simple two-level atom approximation. In this case, the line source function is given by

$$S(r) = [1 - \epsilon(r)]\bar{J}(r) + \epsilon(r)B(r), \quad (6)$$

where $B(r)$ is the local Planck function and $\epsilon(r)$ is the destruction probability, i.e., the ratio of collisional to total deexcitation rates:

$$\epsilon(r) = \frac{C_{ul} N_e(r)}{C_{ul} N_e(r) + A_{ul}}, \quad (7)$$

where C_{ul} is the collision rate per electron, A_{ul} is the Einstein coefficient of the transition, and N_e is the electron density. With the mean intensity calculated from the Sobolev approximation, the source function can be determined given the populations of the two levels. Since the extended Sobolev method includes a nonlocal term (eq. [4]) that itself depends on the source function, the solution must be determined iteratively.

This two-level atom approach is inadequate in that interactions with multiple upper or lower levels, which can significantly affect how a given level is populated, are ignored.

Thus, we have modified the original HHC model by including a multilevel statistical equilibrium calculation. The source function for each line transition in this scheme is given by

$$S_{ul} = \frac{2h\nu_{ul}^3}{c^2} \left[\left(\frac{N_l g_u}{N_u g_l} \right) - 1 \right]^{-1}, \quad (8)$$

where N_l , N_u , g_l , and g_u are the populations and degeneracy factors of the upper and lower levels, respectively, of the transition. The line source functions are then iterated with the populations in statistical equilibrium, allowing us to obtain self-consistently model profiles of as many line transitions as possible given the number of atomic levels used (all results presented here were calculated using an eight-level atom).

The improved method, hereafter referred to as *cvmulti*, uses the system of statistical equilibrium equations of the form

$$-\sum_{j<i} N_j (R_{ji} + C_{ji}) + N_i \times \left[\sum_{j<i} \left(\frac{N_j}{N_i} \right)^* (R_{ij} + C_{ji}) + \sum_{k>i} (R_{ik} + C_{ik}) \right] - \sum_{k>i} N_k \left(\frac{N_i}{N_k} \right)^* (R_{ki} + C_{ik}) = 0, \quad (9)$$

(Mihalas 1978), where R and C are the radiative and collisional transition rates, respectively, for each bound state, i . The starred quantities indicate population ratios in LTE, as given by the Boltzmann equation, and k refers to the continuum. These equations are highly nonlinear, since they depend in part on the radiation field and electron density, which in turn depend on the level populations (see eqs. [1] and [8]). We have used a multiple iteration scheme, with separate iterations for the electron density, level populations, and radiation field. The details of this procedure are given in § 2.2.4. In order to facilitate the solution of the rate equations, we employed an alternate form using departure coefficients, based on the procedure outlined in detail in Vernazza, Avrett & Loeser (1973).

2.2.2. Transition Rates

The rate equation coefficients are set up as follows. The collisional transition rates are given by

$$N_i C_{ij} = N_i N_e \Omega_{ij}(T) \exp(-h\nu_{ij}), \quad (10)$$

$$N_j C_{ji} = N_j \left(\frac{N_i}{N_j} \right)^* C_{ij}, \quad (11)$$

for level $i < j$. The collisional coefficients, $\Omega_{ij}(T)$, are all culled from Johnson (1972) except for the 2–1 transition (from Scholz et al. 1990) and the 3–1 and 3–2 transitions (from Giovanardi, Natta, & Palla 1987) (Chang, Avrett, & Loeser 1991 found the latter to be more accurate).

The radiative bound-bound excitation and de-excitation rates are given by

$$N_i R_{ij} = N_i B_{ij} \bar{J}_{ij} \quad (12)$$

and

$$N_j R_{ji} = N_j (A_{ji} + B_{ji} \bar{J}_{ij}), \quad (13)$$

where B_{ij} is the stimulated absorption coefficient, A_{ji} and B_{ji} are the stimulated and spontaneous emission coefficients, respectively, and \bar{J}_{ij} is the integrated mean intensity.

The net rate from the upper level j to level i is then

$$N_j(A_{ji} + B_{ji}\bar{J}_{ij}) - N_i B_{ij}\bar{J}_{ij} \equiv N_j A_{ji} Z_{ji} \quad (14)$$

(Mihalas 1978). Solving for Z_{ji} , the net radiative bracket, we get

$$Z_{ji} = 1 - \bar{J}_{ij} \frac{(N_i B_{ij} - N_j B_{ji})}{N_j A_{ji}} = 1 - \left(\frac{\bar{J}_{ij}}{S_{ij}} \right), \quad (15)$$

where S_{ij} is the line source function as given in equation (8), and \bar{J}_{ij} is the mean intensity as given in equation (1). Including the net radiative bracket in the rate equations, in place of the individual excitation and de-excitation rates, significantly speeds up solution convergence.

Finally, we need the bound-free radiative rates. The photoionization rate is

$$N_\kappa R_{\kappa i} = 4\pi \int_{\nu_0}^{\infty} \frac{\alpha_\nu}{h\nu} \left(\frac{2h\nu^3}{c^2} + J_\nu \right) e^{-h\nu/kT} d\nu, \quad (16)$$

where ν_0 is the threshold frequency for a given lower bound level. The photoionization cross section is given by

$$\alpha_\nu = \alpha_{\nu_0} \left(\frac{\nu_0}{\nu} \right)^3. \quad (17)$$

If we approximate the radiation field as a blackbody at the local temperature, T , the integral can be written in terms of the first exponential integral. We then obtain

$$N_\kappa R_{\kappa i} = \frac{8\pi}{c^2} \alpha_{\nu_0} \nu_0^3 E_1 \left(\frac{h\nu_0}{kT} \right). \quad (18)$$

The photoionization rate is

$$N_i R_{ik} = N_i 4\pi \int_{\nu_0}^{\infty} \frac{\alpha_{ik}(\nu)}{h\nu} J_\nu d\nu. \quad (19)$$

We once again simplify the integral by approximating the ionizing radiation field as a blackbody, this time characterized by a specified radiation temperature, T_r . We must also account for the fact that the ionizing continuum, essentially the photosphere plus hot accretion shock, subtends a solid angle of less than 2π at any point on the grid. Thus we include a dilution factor, W , defined as

$$W = \frac{\omega_*}{4\pi} = \frac{1}{2} \left\{ 1 - \left[1 - \left(\frac{R_*}{R} \right)^2 \right]^{1/2} \right\}, \quad (20)$$

where ω_* is the solid angle subtended by the star, R is the distance of the grid point from the center of the star, and R_* is the stellar radius (Mihalas 1978). The characteristic radiation temperature is calculated as a weighted sum of the characteristic blackbody temperatures of the stellar photosphere and accretion shock. Given the dilution factors for the two components, W_{phot} and W_{ring} , we have

$$T_r = T_{\text{phot}} \frac{W_{\text{phot}}}{W_{\text{phot}} + W_{\text{ring}}} + T_{\text{ring}} \frac{W_{\text{ring}}}{W_{\text{phot}} + W_{\text{ring}}}. \quad (21)$$

Finally, given $J_\nu \sim WB_\nu(T_r)$, the integral reduces down to the exponential integral of order 1:

$$N_i R_{ik} = N_i W \frac{8\pi}{c^2} \alpha_{\nu_0} \nu_0^3 E_1 \left(\frac{h\nu_0}{kT_r} \right). \quad (22)$$

2.2.3. Electron Density

The original model of HHC used a fixed contribution from metals; here, we calculate the metal contribution from

the first two ionization stages of all elements up to iron, using the appropriate abundances and assuming LTE. The total electron density is then the sum of the hydrogen continuum population (protons) plus the total number of ionizations (electrons) from the metals. Since the rate equations depend on the electron density through the expressions for the collision rates, the solution for the electron density must be iterated in tandem with the level populations. An initial value for N_e is assumed, the level populations are calculated, then from N_κ a new value of N_e is calculated, and the process repeats until the solution for N_e converges.

2.2.4. Iteration Procedure

The set of statistical equilibrium equations in general matrix form (as adapted from eq. [9]) is

$$\mathbf{P} \cdot \mathbf{b} = 0, \quad (23)$$

where $\mathbf{P} = \{P_{ij}\}$, an array containing the total rate coefficients for transitions ij , and $\mathbf{b} = \{b_j\}$, the vector of departure coefficients for each level j . The system is solved using a standard LU decomposition routine. To start the entire procedure, we need initial values for the level populations, N_i , the electron density, N_e , and the net radiative bracket, Z_{ij} . Populations from a previous case with parameters similar to the current run are used for initial values. For the first case run, values for N_1 , N_2 , and N_e from initial models run with the original HHC version were used, and the upper level populations were derived from LTE arguments. Once the level populations are found, the source function (eq. [8]) can be determined at each point. With the new source function, the mean intensity of the radiation field (eq. [1]), and then new values of the radiative transition rates, can be calculated. This process is likewise repeated until the solution for the populations (or, more precisely, the departure coefficients) converges, forming the primary iteration loop of the multilevel line transfer treatment.

3. RESULTS

3.1. Profiles

To compare with the results of HHC, we first consider the same stellar and magnetospheric parameters. HHC used a star of mass $0.8 M_\odot$, radius $2 R_\odot$, and photospheric temperature 4000 K. Their magnetosphere had an inner and outer radius of $2.2R_*$ and $3R_*$, respectively, a temperature distribution with a maximum at about 7500 K, an accretion rate of $10^{-7} M_\odot \text{ yr}^{-1}$, and an accretion shock temperature of 7200 K. Figure 4 compares the HHC profiles with ones generated with *cvmulti* for an eight-level atom. The general profile shape is nearly identical in both cases, but the *cvmulti* lines are about 50% less in equivalent width, and the redshifted absorption feature is somewhat more pronounced. The decrease in line strength is due to the presence of multiple upper levels to which the $n = 2$ level can give up electrons, leading to a lower line optical depth and a lower source function.

The qualitative shape of the Balmer line profiles is largely due to the velocity field and the geometry of the system. The line widths increase with inclination angle, as the line of sight becomes more aligned with the fastest parts of the flow. The redshifted absorption component likewise becomes more prominent at higher inclinations, since the line of sight to the hot accretion shock passes through an increasing amount of infalling material. Emission at low velocities comes from both the regions of the flow nearest

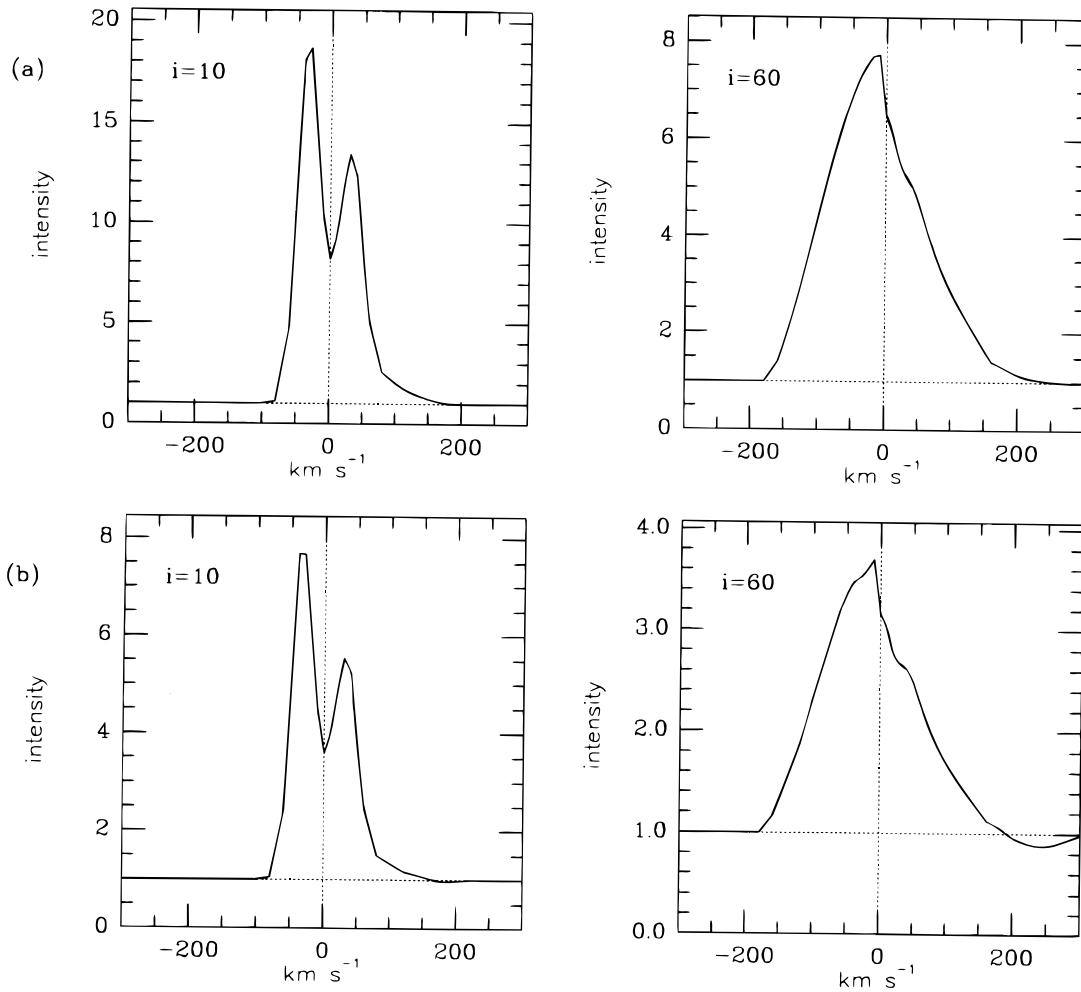


FIG. 4.—Comparison of H α profiles for the case of $\dot{M} = 10^{-7} M_{\odot} \text{ yr}^{-1}$, $T_{\text{max}} = 7500 \text{ K}$, $R_* = 2 R_{\odot}$, $M_* = 0.8 M_{\odot}$, $r_{\text{mi}} = 2.2 R_{\odot}$, and $r_{\text{mo}} = 3 R_{\odot}$ for (a) HHC results and (b) *cvmulti* results.

the disk and from material moving essentially perpendicular to the line of sight. This is by far the largest emitting volume and explains the centrally peaked nature of the profiles.

The multilevel atom model enables us to calculate, self-consistently, profiles in line series other than Balmer. Figure 5 shows model profiles of Br γ for an eight-level atom. These lines exhibit the same qualitative shape as the Balmer lines, suggesting a common emitting region. One might expect the Paschen and Brackett lines to form in a more limited volume of the magnetosphere closer to the star, since they are more difficult to excite than the Balmer lines. This would cause the profiles to be of a different shape. However, even these infrared lines have large optical depths over most of the magnetosphere for this particular set of parameters, and so their profiles are consistent with being optically thick. (This is not strictly true at lower accretion rates and gas temperatures, however; see the next section).

3.2. Parameter Dependence of Line Fluxes

We have explored parameter space by varying the accretion rate, gas temperature (characterized by the maximum value of the distribution), and the width and radial extent of the magnetosphere. In each case, one of these parameters is changed while the others are held fixed; however, we note that the parameters are not completely independent in all

cases. For example, consider a magnetosphere with $R_i = 4 R_{\odot}$, $R_o = 6 R_{\odot}$ (Fig. 3); T_{max} and the accretion rate are the same as in the fiducial case (Fig. 2). The infall velocity at a given point is larger than in the fiducial case, since material is falling from a greater distance. Also, the cross-sectional area is larger near the disk and smaller near the star. These two factors conspire to change the density distribution even though the accretion rate is the same. Similarly, the temperature distribution changes somewhat for a given T_{max} : the temperature is lower near the disk since the volume is greater, and hence there is less heating; the temperature is lower near the star since the density is higher, and hence there is more radiative cooling.

In each case, we calculate the total line flux by adding the emergent flux per unit frequency (eq. [5]) over the width of the line, subtracting the contribution from the continuum. We present model line fluxes for five hydrogen lines for a range of parameters in Table 1. Figures 6–7 show how the model line flux varies with the main parameters discussed above for H α (the other lines exhibit similar behavior, albeit at generally lower fluxes). Some of the fluxes are negative at low accretion rates and temperatures (i.e., the line is in absorption) and have not been plotted. In these cases, the redshifted absorption component is dominant over the part of the line in emission (which is either flat topped or virtually nonexistent). This type of behavior has not been

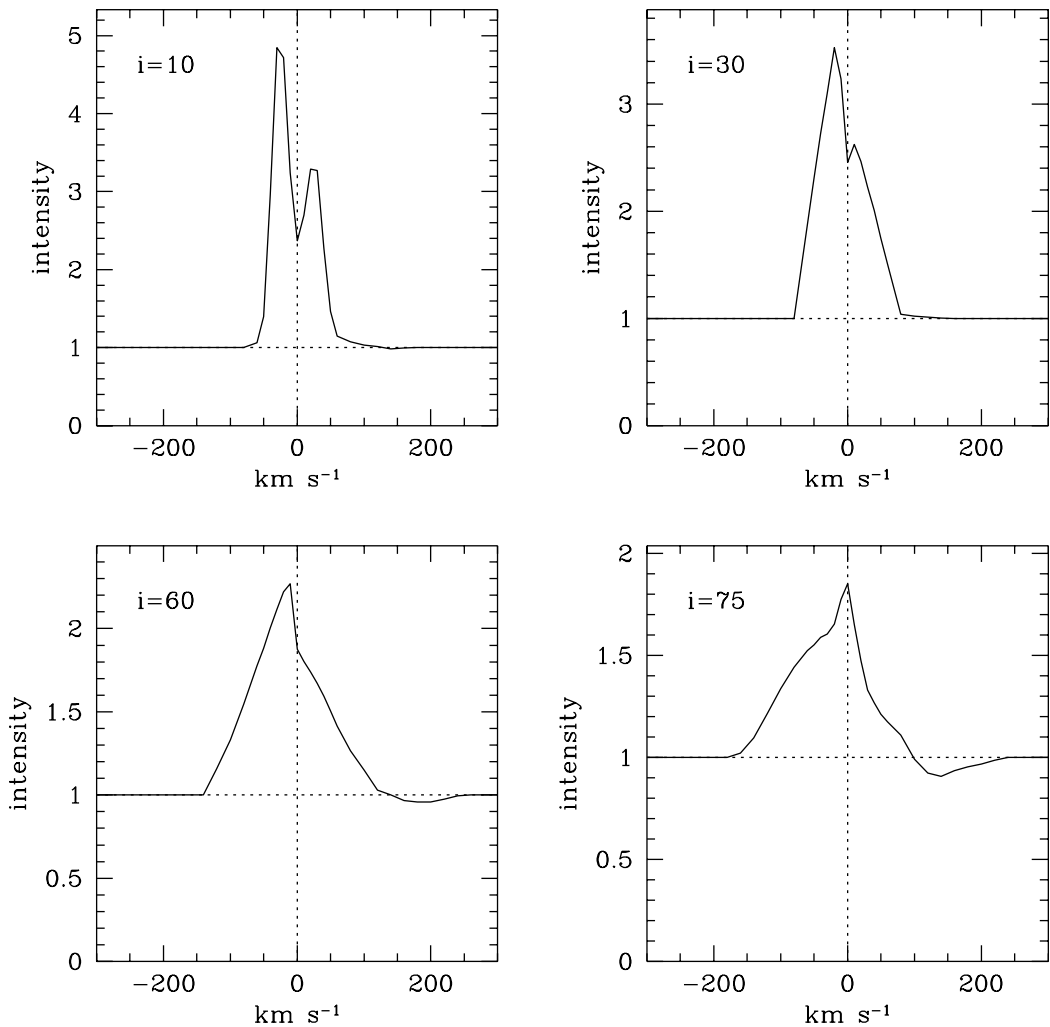


FIG. 5.—Br γ profiles with the fiducial parameters ($\dot{M} = 10^{-7} M_{\odot} \text{ yr}^{-1}$, $T_{\text{max}} = 8000 \text{ K}$, $R_{*} = 2 R_{\odot}$, $M_{*} = 0.5 M_{\odot}$, $r_{\text{mi}} = 2.2 R_{*}$, and $r_{\text{mo}} = 3 R_{*}$).

observed in CTTs, which indicates a possible constraint on temperature (see discussion).

The model results can be separated into two regions in density space. (1) At low accretion rates, the flux decreases

dramatically with decreasing accretion rate because there is a fairly sharp drop in the line optical depth, and the emission essentially goes away (this behavior is especially striking in the line profiles, which become either flat topped or

TABLE 1
MODEL PARAMETERS AND LINE FLUXES

LOG \dot{M} ($M_{\odot} \text{ yr}^{-1}$)	T_{max} (K)	r_{mi} (R_{*})	r_{mo} (R_{*})	LOG LINE FLUX ($\text{ergs cm}^{-2} \text{ s}^{-1}$)				
				H α	H β	H γ	Pa β	Br γ
−6.....	8000	2.2	3	7.51	7.39	7.30	7.06	6.66
−7.....	8000	2.2	3	7.39	7.16	6.88	6.75	6.34
−8.....	8000	2.2	3	7.17	6.80	6.52	6.34	5.87
−9.....	8000	2.2	3	6.19	5.39	4.94	...	4.15
−6.....	10000	2.2	3	7.88	7.95	7.95	7.44	6.95
−7.....	10000	2.2	3	7.60	7.49	7.40	7.09	6.71
−8.....	10000	2.2	3	7.50	7.25	7.04	6.77	6.38
−9.....	10000	2.2	3	7.11	6.59	6.09	6.06	5.28
−6.....	8000	4	6	8.02	7.80	7.62	7.46	7.09
−7.....	8000	4	6	7.95	7.62	7.33	7.22	6.82
−8.....	8000	4	6	7.19	6.52	6.24	5.90	5.10
−9.....	8000	4	6	5.76	5.02	4.39	4.50	4.29
−6.....	10000	4	6	8.31	8.31	8.28	7.88	7.45
−7.....	10000	4	6	8.13	7.92	7.75	7.50	7.12
−8.....	10000	4	6	8.06	7.76	7.48	7.26	6.84
−9.....	10000	4	6	7.21	6.37	5.81	5.69	4.13

NOTE.—All results are for $M_{*} = 0.5 M_{\odot}$ and $R_{*} = 2 R_{\odot}$.

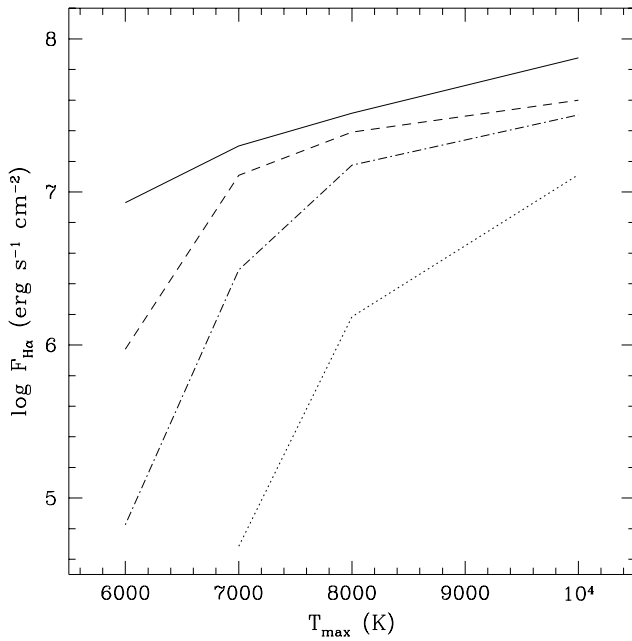


FIG. 6.—Model H α line fluxes for various temperature distributions (as defined by the maximum temperature) and accretion rates for a magnetosphere with $r_{\text{mi}} = 2.2R_*$ and $r_{\text{mo}} = 3R_*$. The models are $\dot{M} = 10^{-6} M_\odot \text{ yr}^{-1}$ (solid line), $\dot{M} = 10^{-7} M_\odot \text{ yr}^{-1}$ (dashed line), $\dot{M} = 10^{-8} M_\odot \text{ yr}^{-1}$ (dash-dotted line), and $\dot{M} = 10^{-9} M_\odot \text{ yr}^{-1}$ (dotted line).

completely in absorption). (2) The slope in the line flux as a function of accretion rate becomes shallower at higher accretion rates because of the increasing thermalization of the lines. Eventually, at high enough densities, the magnetosphere would become a completely optically thick blackbody, with the emergent flux coming only from the outer surface. Because of this behavior, the H α line fluxes would only be good accretion rate indicators for objects with the lowest accretion rates.

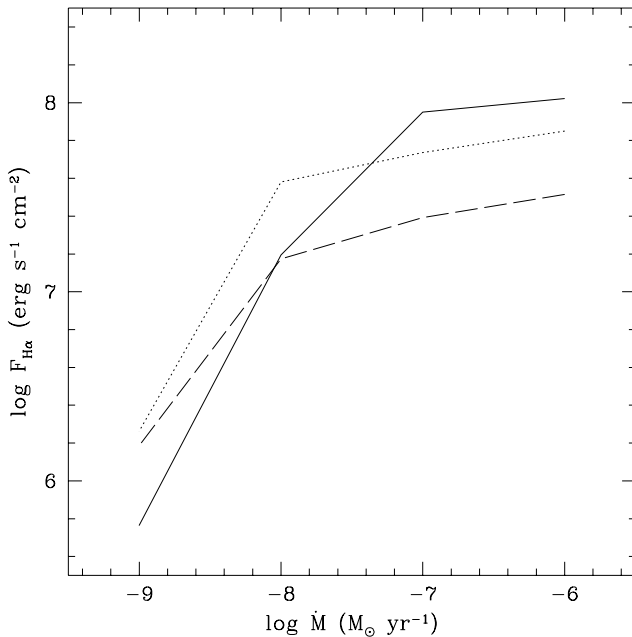


FIG. 7.—Model H α line fluxes as a function of accretion rate. The model values are $r_{\text{mi}} = 4R_*$ and $r_{\text{mo}} = 6R_*$ (solid line); $r_{\text{mi}} = 5.2R_*$ and $r_{\text{mo}} = 6R_*$ (dotted line); and $r_{\text{mi}} = 2.2R_*$ and $r_{\text{mo}} = 3R_*$ (dashed line). In each case, $T_{\text{max}} = 8000 \text{ K}$.

The critical point at which the flux begins to decrease sharply with decreasing density occurs at higher accretion rates the lower the gas temperature becomes. Line thermalization depends on both the density and temperature of the gas; thus, if one parameter is low, the other must be correspondingly higher for the line to be very optically thick. For the temperature distribution with $T_{\text{max}} = 6000 \text{ K}$, the line emission is either very low or not present for all but the highest accretion rates ($10^{-6} M_\odot \text{ yr}^{-1}$), whereas for the distribution with $T_{\text{max}} = 10,000 \text{ K}$, the emission is in the very optically thick regime for accretion rates as low as $10^{-8} M_\odot \text{ yr}^{-1}$. Note that the temperature has a significant effect on the line flux over the entire range of density, especially at the lowest accretion rates. Thus, we must have independent constraints of the temperature (see discussion).

The size of the infall region also significantly affects the line flux, especially in the thermalization regime. Figure 7 shows the line flux versus accretion rate for two cases with the same magnetospheric thickness but different outer radii (small/narrow and large/narrow magnetospheres) and two cases with the same outer radii but different thicknesses (large/narrow and large/wide magnetospheres). There are two main effects here. First, the narrow cases are thermalized as low as $10^{-8} M_\odot \text{ yr}^{-1}$, whereas the line flux in the large/wide case drops off at a higher accretion rate. This is a consequence of the change in volume, where a larger volume translates to lower densities over most of the magnetosphere for a given accretion rate (compare Figs. 2 and 3). Second, both the width and the outer radius are important; increasing either of these parameters significantly increases the line flux in the thermalization regime. Unfortunately, we may not be able to discriminate between the inner and outer radius of the infall zone from the models alone, although we may be able to constrain the inner radius from independent estimates of the disk hole size.

3.3. Comparison with Observations

Figures 8–10 show the model line fluxes for various cases as a function of accretion rate superposed on observed values for a number of CTTs in Taurus. H α line fluxes are taken from Kuhl (1974)—a more recent set of observations for a similarly large sample is sorely lacking. To plot these, we used reddening magnitudes and accretion rates from GHBC, except for five stars (CI Tau, DL Tau, DG Tau, DR Tau, and RW Aur) for which GHBC could not measure A_V or the accretion rate owing to the extremely high veiling. The only published values for the extinction and accretion rate of DG Tau and DR Tau are from Hartigan, Edwards, & Ghandour (1995; hereafter, HEG). For the rest, we use values from Valenti, Basri, & Johns (1993; hereafter VBJ), since their results are more consistent with GHBC (see GHBC). Lacking a consistent data set for H α , we will not focus on comparing with the models. We also note that the line flux of DR Tau observed 25 years ago is inconsistent with its recently derived accretion rate. A significant brightening occurred in the interim (Chavarria 1979), and thus its present H α flux is surely much higher. Dereddened line fluxes and accretion rates for H β and H γ (Figs. 9 and 10) are from GHBC. The data from GHBC are especially useful because all of the quantities for each object (line fluxes, reddening, and accretion rates) are derived simultaneously from the same spectrum. The lack of published line fluxes for a sample of objects with a wide range of accretion rates prevents a thorough comparison of the infrared lines. We

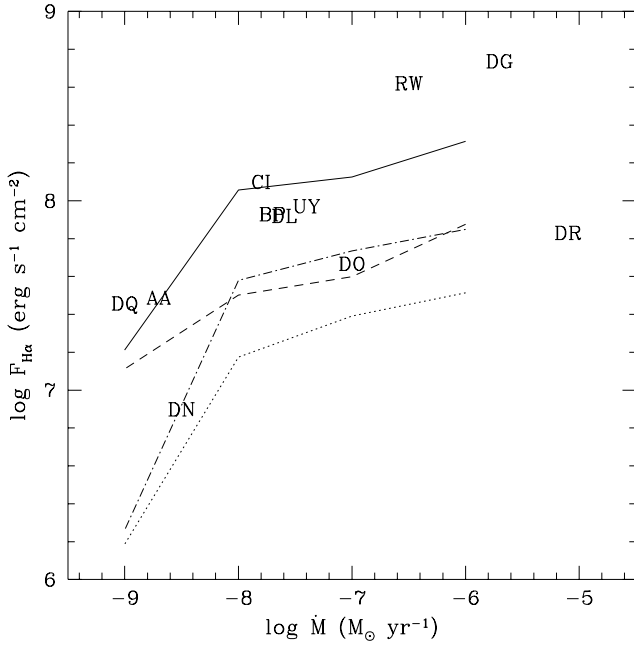


FIG. 8.—Integrated $H\alpha$ line flux vs. accretion rate for selected CTTSs in Taurus. Observed data are delineated by the first two letters of the star name. Line fluxes are from Kuhl (1974), dereddened with A_V from GHBC except DL Tau, CI Tau, and RW Tau from VBJ and DR Tau and DG Tau from HEG. Accretion rates are from GHBC, with the same exceptions (see text). All models have $M_* = 0.5 M_\odot$, $R_* = 2 R_\odot$. The dotted line is for $r_{mi} = 2.2R_*$, $r_{mo} = 3R_*$, and $T_{max} = 8000$ K; the dash-dotted line, $r_{mi} = 4R_*$, $r_{mo} = 6R_*$, and $T_{max} = 8000$ K; the dashed line, $r_{mi} = 2.2R_*$, $r_{mo} = 3R_*$, and $T_{max} = 10,000$ K; and the solid line, $r_{mi} = 4R_*$, $r_{mo} = 6R_*$, and $T_{max} = 10,000$ K.

therefore concentrate our analysis on the upper Balmer lines.

Our goal is to determine if the magnetospheric model can explain the observed range of line fluxes and accretion rate estimates and proceed to constrain the uncertain magnetospheric physical parameters (size, width, temperature).

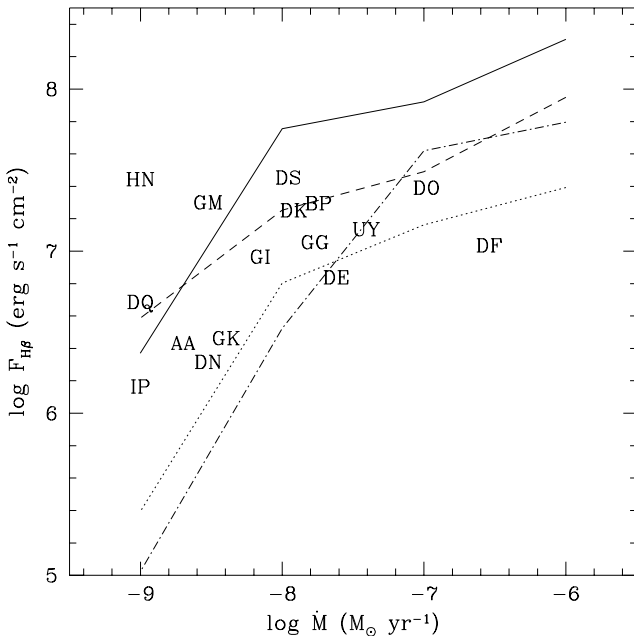


FIG. 9.—Integrated $H\beta$ line flux vs. accretion rate. Observed dereddened line fluxes and accretion rates from GHBC. See Fig. 8 for model parameters.

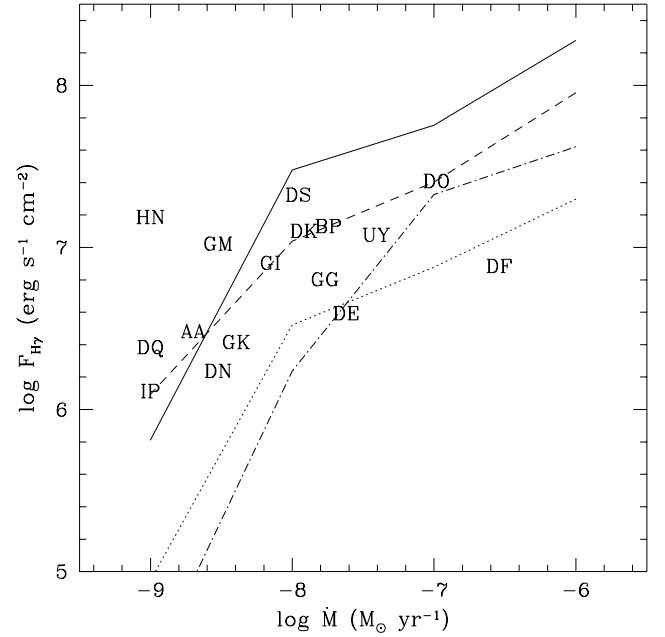


FIG. 10.—Integrated $H\gamma$ line flux vs. accretion rate. Observed dereddened line fluxes and accretion rates from GHBC. See Fig. 8 for model parameters.

Comparing the models to the *simultaneous* data set of GHBC enables us to do this with a fair degree of confidence. We make the following qualitative conclusions based on the $H\beta$ and $H\gamma$ comparison plots. (1) The observed spread in line flux at a given accretion rate is accounted for with an acceptable range of model parameters (sizes consistent with observational estimates of disk hole sizes and corotation radii; L. Hillenbrand 1996, private communication; see § 4.1 for a discussion of the temperature). (2) Objects with low accretion rates may have magnetospheric temperatures higher ($T \sim 10,000$ K) than objects with higher accretion rates ($T \sim 8000$ K), although a more exact constraint cannot be made from these lines alone because differences in magnetospheric sizes and widths are also important.

There are some discrepancies between the models and the data that must be addressed. For instance, the $H\beta/H\gamma$ ratio (Fig. 11) is not consistent for the entire range of observed accretion rates. Many objects with low accretion rates (including IP Tau, DN Tau, GK Tau, and AA Tau) have smaller $H\beta/H\gamma$ ratios than the models predict. A likely source of additional line emission (not included in this treatment) is the hot accretion shock. The shock region is small, and the Balmer decrements should be close to 1 (as in the case of chromospheres—see Calvet, Basri, & Kuhl 1984), while the Balmer decrement is larger in the magnetosphere, since the emitting region is much larger. Shock line emission may be overwhelmed by the magnetospheric contribution for all but the lowest accretion rates, hence its effects are only seen in objects with low accretion rates. More detailed calculations including the accretion shock are currently underway.

Another discrepancy is that high-resolution spectroscopy of the Balmer lines (Edwards et al. 1994) shows that the $H\alpha$ profiles of most CTTSs exhibit extended high-velocity wings (out to as much as ± 500 km s $^{-1}$). This may well not represent high-velocity material but instead Stark line broadening, which our calculations do not take into account. One would expect Stark wings to be important in

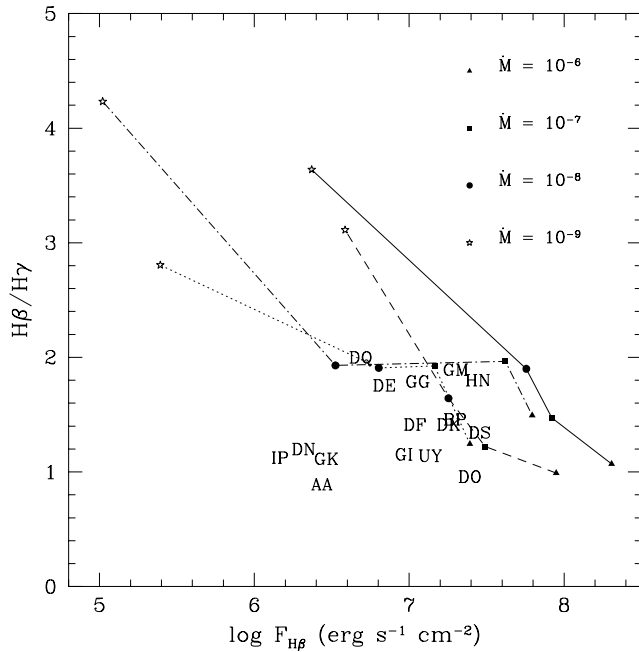


FIG. 11.—Balmer line flux ratio vs. line flux. Model results are all for $M_* = 0.5 M_\odot$ and $R_* = 2 R_\odot$. The dotted line is for $r_{\text{mi}} = 2.2R_*$, $r_{\text{mo}} = 3R_*$, and $T_{\text{max}} = 8000$ K; the dash-dotted line, $r_{\text{mi}} = 4R_*$, $r_{\text{mo}} = 6R_*$, and $T_{\text{max}} = 8000$ K; the dashed line, $r_{\text{mi}} = 2.2R_*$, $r_{\text{mo}} = 3R_*$, and $T_{\text{max}} = 10,000$ K; and the solid line, $r_{\text{mi}} = 4R_*$, $r_{\text{mo}} = 6R_*$, and $T_{\text{max}} = 10,000$ K. Observational data are from GHBC, with objects labeled as in Figs. 8–10.

$H\alpha$, since the line optical depths are so high ($>10^4$). We present preliminary results of line broadening using a simple slab model in § 4.2. Finally, we point out that the applicability of the magnetospheric accretion model is in doubt for those CTTs with the highest accretion rates. Stars with very high implied accretion rates, such as DR Tau and RW Aur, have extremely active outflowing winds. The presence of strong winds is implied from the considerable blueshifted absorption seen in the Balmer line profiles, and strong jets have also been observed in $H\alpha$ in several of these objects (Hirth et al. 1994). Thus, the observed $H\alpha$ line fluxes may be strongly affected by these additional sources.

We would like to compare model and observational results for the infrared lines. Unfortunately, relatively few line fluxes have been published and then only for objects with the highest accretion rates. However, high-resolution line profiles have been recently obtained, most notably in Najita, Carr, & Tokunaga (1996; hereafter, NCT) and Folha, Emerson, & Calvet (1997); thus, we can at least compare observed and model line profiles, if not fluxes. Figure 12 compares an observed high-resolution line profile of $\text{Br}\gamma$ from NCT to a model profile with typical CTTs parameters. The match to the WL 16 $\text{Br}\gamma$ profile is of special interest, since the source is an embedded object. Determinations of the accretion rate of such objects using the standard veiling techniques are impossible because of the large extinction. We estimate the accretion rate by assuming the bolometric luminosity of WL 16 is due entirely to accretion and obtain a value of about $10^{-5.5} M_\odot \text{ yr}^{-1}$ (again, using standard T Tauri star parameters). Our match to the observed profile uses an accretion rate of $10^{-6} M_\odot \text{ yr}^{-1}$ and has a total line flux fairly similar to the value determined by NCT (about $2.4 \times 10^6 \text{ ergs cm}^{-2} \text{ s}^{-1}$). The model line is somewhat narrower than the observed profile; we are currently exploring models with a higher mass star (NCT

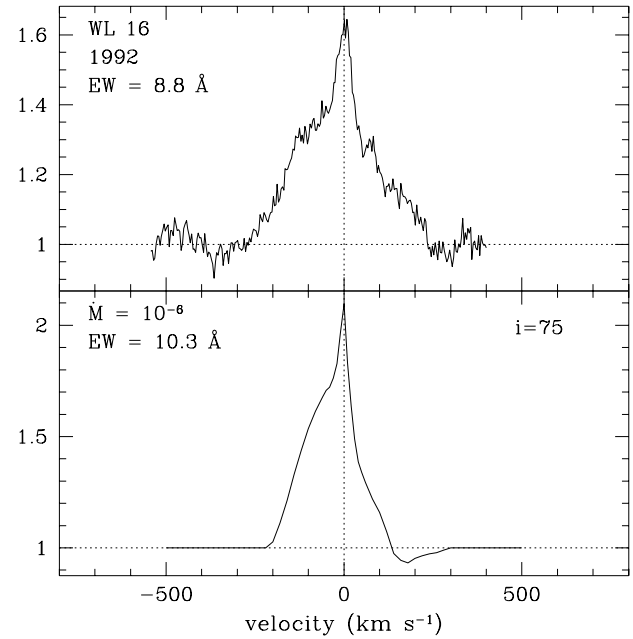


FIG. 12.—Comparison of model $\text{Br}\gamma$ profile with observed profile for the embedded object WL 16 from NCT.

estimates a value of about $2.5 M_\odot$ for WL 16), which should increase the line width since the gas infall velocities will increase.

This result is encouraging in light of our goal of applying the model as a diagnostic tool for embedded CTTs, although the line thermalization problem we see in the Balmer lines is also present (albeit to a lesser degree) in $\text{Br}\gamma$, and thus this line may not prove to be a useful accretion rate indicator. However, more determinations of line fluxes for lightly extincted objects, over a wide range of accretion rates, are essential to establishing a possible accretion rate calibration with this line (or others, like $\text{Pa}\beta$). Nevertheless, a significant implication of this profile match is that magnetospheric accretion seems to occur at earlier evolutionary phases and in higher mass objects than the classical T Tauri stars.

4. DISCUSSION

4.1. Constraining the Temperature

The temperature structure of the magnetosphere is one of the biggest uncertainties in the magnetospheric accretion model. No one has put forth a theory for heating the infalling gas until recently. Martin (1996) performs a full thermodynamic treatment of the infalling gas, using the same physical parameters as HHC. A variety of heating sources are considered, including Balmer photoionization and adiabatic compression due to the converging field lines (which turns out to be the dominant source). The cooling is dominated by Ca II and Mg II line emission. Martin obtains a temperature distribution that increases as the field lines converge and compressional heating increases and levels off at a certain point where the cooling from the ion emission becomes important. We find that this temperature distribution is inadequate to obtain line emission consistent with the observations, even at $H\alpha$; our models suggest mean temperatures no less than about 6000 K are required. Martin's temperature distribution attains a maximum at about this temperature, but that only occurs in a limited

volume of gas close to the star—the mean is much lower (4000–5000 K). There must be another, stronger heating source that has not been considered. In fact, Martin (1996) does not include any magnetically driven effects, which seem likely to be important, if not dominant, in any magnetospheric accretion scheme.

We have retained the same crude temperature distribution used by HHC, since a satisfactory theoretical basis for magnetospheric heating has yet to be established. As HHC point out, this distribution gives line profiles in general agreement with the observations, whereas, for instance, an isothermal structure produces far too much emission from the part of the magnetosphere near the disk. The ad hoc nature of the temperature distribution must be taken into account when considering the results, both in the behavior of the line flux and in the appearance of the line profiles. However, comparison with the observations allows us to put some constraints on the temperature.

The line profiles and fluxes prove to be quite useful in this regard. If the temperature is too low, the gas is not sufficiently excited to produce the emission that is observed. This is especially true in the low-velocity regions of the flow, where the temperature distribution dips. Model cases for a maximum temperature of 6000 K show flat-topped line profiles at high accretion rates ($> 10^{-8} M_{\odot} \text{ yr}^{-1}$) and virtually no emission at low accretion rates. In fact, for low accretion rates, there is little line emission until temperatures reach about 8000–9000 K. This does not match any of the observations, and so indicates a lower bound to the temperature range necessary to reproduce the observations.

Likewise, we attempt to estimate an upper limit to the temperature by examining the gas continuum optical depth. If the gas temperature is too high, the continuum will become optically thick, effectively covering up the line emission. This is at odds with the observations, which show that even objects with very high accretion rates (hence high densities) exhibit strong line emission. Thus, in all cases, the continuum should be optically thin. We find approximate upper limits of 7000 K for high accretion rates ($10^{-6} M_{\odot} \text{ yr}^{-1}$) and 10,000 K for low accretion rates ($10^{-8} M_{\odot} \text{ yr}^{-1}$). Figure 13 delineates the allowed temperature regime with these upper and lower bounds.

4.2. Effects of Stark Broadening

One of the major discrepancies between the model results and the observations is the $H\alpha$ emission. As it is currently implemented, the model is not able to reproduce the substantial line wings (typically $\pm 500 \text{ km s}^{-1}$) seen in the $H\alpha$ profiles of many CTTs. As previously suggested, given the very large optical depths involved, a likely source of the broad wings is Stark broadening.

We performed a rough calculation of the line-damping wings with a simple isothermal and uniform slab model. Taking into account the Voigt profile, given by

$$H(a, v) = \frac{a}{\pi} \int_{-\infty}^{\infty} \frac{e^{-y^2} dy}{(v - y)^2 + a^2} \quad (24)$$

(Mihalas 1978), where $v = (v - v_0)/\Delta v_D$, $y = \Delta v/\Delta v_D$, and $a = \Gamma/4\pi\Delta v_D$, the line absorption coefficient becomes

$$\kappa_v = \frac{\pi^{1/2} e^2}{mc} \frac{f}{\Delta v_D} N_l \left(1 - \frac{g_l N_u}{g_u N_l} \right) H(a, v). \quad (25)$$

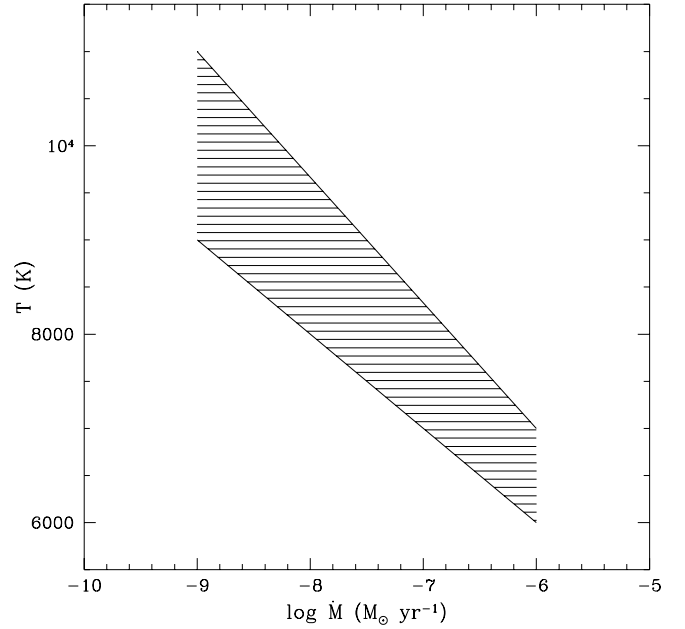


FIG. 13.—Region of allowed mean gas temperatures, as a function of accretion rate, from the constraints discussed in the text.

Following the prescription used by Vernazza et al. (1973), we calculate the damping constant, Γ , with

$$\Gamma = C_{\text{rad}} + C_{\text{vdW}} \left(\frac{n_{\text{HI}}}{10^{16} \text{ cm}^{-3}} \right) \left(\frac{T}{5000 \text{ K}} \right)^{0.3} + C_{\text{Stark}} \left(\frac{N_e}{10^{12} \text{ cm}^{-2}} \right)^{2/3}, \quad (26)$$

where C_{rad} , C_{vdW} , and C_{Stark} are the radiative, van der Waals, and Stark half-widths, respectively.

We compare the relative contribution from the damping wings, as calculated from the slab models, to the total line flux as calculated from the *cvmulti* models. Figure 14 plots the ratio of the net flux from the broadening component (with the Doppler core subtracted out) to the total line flux as a function of temperature and density. In each slab calculation, we used the approximate mean value of the density distribution and the maximum temperature of the temperature distribution from each of the *cvmulti* cases. Since the density and temperature actually varies with radius in the magnetospheric model, comparison with the isothermal, constant density slab are only approximate. These rough results indicate that the contribution from Stark broadening from the infalling gas is small for all but the largest accretion rates ($\geq 10^{-6} M_{\odot} \text{ yr}^{-1}$). However, we are now exploring other regions in which the line wings may form. For example, the postshock region of the hot accretion shock has $n_{\text{H}} > 10^{12} \text{ cm}^{-3}$ and $T \sim 10,000 \text{ K}$ (Hartigan et al. 1991; VBJ), which is well within the range for significant Stark broadening shown with the slab model. Similar calculations for $H\beta$ show that the upper Balmer lines are not as strongly affected by Stark broadening in these temperature and density regimes (the contribution is about 50% less than in $H\alpha$), which is consistent with the data.

4.3. Accretion Rate Diagnostics

One of the ultimate goals in studying the emission lines is to obtain some diagnostic of the accretion rate. Unfortunately, there are several complications that prevent us

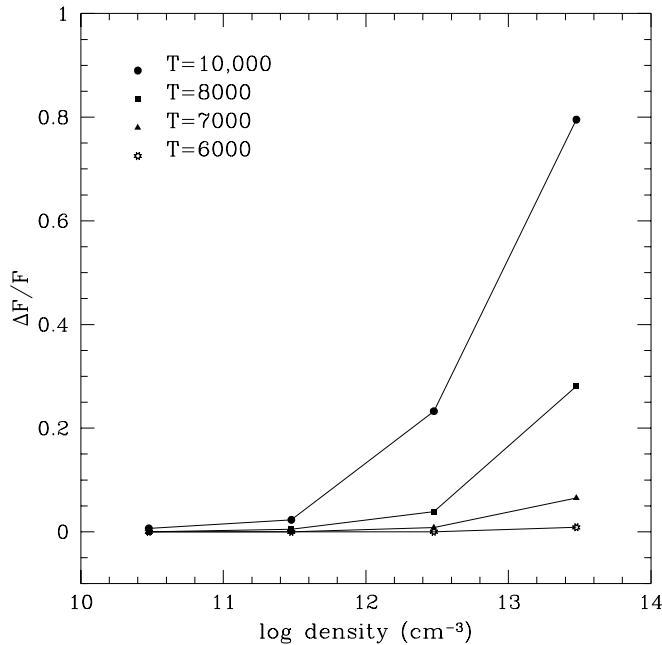


FIG. 14.—Ratio of the net slab model line flux from Stark broadening to the total magnetospheric model line flux, for H α .

from developing a straightforward calibration using the line fluxes alone. We have previously shown that the temperature and size (including both the outer radius and width) of the magnetosphere are important factors in producing the line emission. Additionally, the Balmer lines and Br γ are all optically thick at higher accretion rates; hence, the total line flux does not greatly depend on the gas density. We need some way of disentangling the effects of all these parameters on the line flux.

We require lines with significantly different excitation conditions, especially more optically *thin* lines. Transitions with high- n upper levels may be useful; recently obtained

data indicate that the last Paschen and Brackett lines visible in emission in a CTTS spectrum may correlate with the accretion rate (the higher the accretion rate, the higher n transition is seen in emission). Modelling of emission lines of other atomic species may also prove useful; observed profiles of some O I and Na I lines, as well as the broad components of He I and Ca II (Hamann & Persson 1992; Gullbring et al. 1996; Johns-Krull & Basri 1997), are in general agreement with the hydrogen magnetospheric profiles. These issues will be addressed in a future paper.

5. CONCLUSION

We have further explored the ability of the magnetospheric accretion model to explain the observed hydrogen line emission from classical T Tauri stars. Implementing a multilevel statistical equilibrium radiative transfer treatment, we are able to improve on the methods of HHC to calculate line profiles and fluxes self-consistently. From these results, we conclude that (1) the model line fluxes and profiles for the Balmer lines are in good agreement with the observations; (2) the observed spread in flux for a given accretion rate is due mostly to differences in the width, radial extent, and temperature of the infall region; (3) the model is able to match observed infrared line profiles from embedded objects, based on our match to the Br γ line of WL16; (4) the temperature of the infalling gas can be constrained to upper and lower limits of about 10,000 and 6000 K, respectively, and should vary inversely with accretion rate; (5) Stark broadening from the postshock region of the accretion shock may contribute to the line wings observed at H α ; and (6) we need models and observations of optically thin lines to obtain definitive emission-line accretion rate diagnostics.

J. M. would like to thank Steve Strom for support and useful discussions. Work supported in part by NASA grants 2306 and NAG 5-4282.

REFERENCES

- Appenzeller, I. & Wolf, B. 1977, A&A, 54, 713
 Bertout, C., Basri, G., & Bouvier, J. 1988, ApJ, 330, 350
 Bouvier, J., Cabrit, S., Fernandez, M., Martin, E., & Matthews, J. 1993, A&A, 272, 176
 Bouvier, J., Covino, E., Kovo, O., Martin, E., Matthews, J., Terranegra, L., & Beck, S. 1995, A&A, 299, 89
 Calvet, N., Basri, G., & Kuhi, L. V. 1984, ApJ, 282, 631
 Calvet, N., & Hartmann, L. 1992, ApJ, 386, 239
 Calvet, N., Hartmann, L., & Hewett, R. 1992, ApJ, 386, 229
 Chang, E. S., Avrett, E. H., & Loeser, R. 1991, A&A, 247, 580
 Chavarria, K. C. 1979, A&A, 79, L18
 Edwards, S. 1979, PASP, 91, 329
 Edwards, S., Hartigan, P., Ghandour, L., & Andrulis, C. 1994, AJ, 108, 1056
 Folha, D., Emerson, J., & Calvet, N. 1997, in Poster Papers, IAU Symp. 182, Low-Mass Star Formation—from Infall to Outflow, ed. F. Malbet & A. Castets (City: Observatoire de Grenoble), 272
 Giovanardi, C., Natta, A., & Palla, F. 1987, A&AS, 70, 269
 Gullbring, E., Hartmann, L., Briceño, C., & Calvet, N. 1998, ApJ, in press (GHBC)
 Gullbring, E., Petrov, P. P., Ilyin, I., Tuominen, I., Gahm, G. F., & Lodén, K. 1996, A&A, 314, 835
 Hamann, F., & Persson, S. E. 1992, ApJS, 82, 247
 Hartigan, P., Edwards, S., & Ghandour, L. 1995, ApJ, 452, 736 (HEG)
 Hartigan, P., Kenyon, S. J., Hartmann, L., Strom, S. E., Edwards, S., Welty, A., & Stauffer, J. 1991, ApJ, 382, 617
 Hartmann, L., Calvet, N., Avrett, E. H., & Loeser, R. 1990, ApJ, 349, 168
 Hartmann, L., Edwards, S., & Avrett, E. 1982, ApJ, 261, 279
 Hartmann, L., Hewett, R., & Calvet, N. 1994, ApJ, 426, 669 (HHC)
 Herbst, W., Herbst, D. K., & Grossman, E. J. 1994, AJ, 108, 1906
 Hirth, G. A., Mundt, R., Solf, J., & Ray, T. P. 1994, ApJ, 427, L99
 Johns-Krull, C. M., & Basri, G. 1997, ApJ, 474, 433
 Johnson, L. C. 1972, ApJ, 174, 227
 Kenyon, S. J., et al. 1994, AJ, 107, 2153
 Königl, A. 1991, ApJ, 370, L39
 Kuhi, L. V. 1974, A&AS, 15, 47
 Martin, S. C. 1996, ApJ, 470, 537
 Mihalas, D. 1978, Stellar Atmospheres (San Francisco: Freeman)
 Najita, J., Carr, J. S., & Tokunaga, A. T. 1996, ApJ, 456, 292 (NCT)
 Rybicki, G. B., & Hummer, D. G. 1978, ApJ, 219, 654
 Scholz, T. T., Walters, H. R. S., Burke, P. G., & Scott, M. P. 1990, MNRAS, 242, 692
 Shu, F., Najita, J., Ostriker, E., & Wilkin, F. 1994, ApJ, 429, 781
 Simon, T., Vrba, F. J., & Herbst, W. 1990, AJ, 100, 1957
 Valenti, J. A., Basri, G., & Johns, C. M. 1993, AJ, 106, 2024 (VBJ)
 Vernazza, J. E., Avrett, E. H., & Loeser, R. 1973, ApJ, 184, 605
 Walker, M. F. 1972, ApJ, 175, 89